RSC Advances

PAPER

View Article Online
View Journal | View Issue

Cite this: *RSC Adv.*, 2019, **9**, 41038

A new flexible and ultralight carbon foam/$Ti_3C_2T_X$ MXene hybrid for high-performance electromagnetic wave absorption

Yang Wang,[ab] Jian Yang,*[ab] Zhaofeng Chen[c] and Yunlong Hu[a]

Received 23rd November 2019
Accepted 6th December 2019

DOI: 10.1039/c9ra09817h

rsc.li/rsc-advances

A new ultralight carbon foam/$Ti_3C_2T_X$ (CF/MXene) electromagnetic (EM) absorbing hybrid with three-dimensional network structure was fabricated by vacuum impregnation and freeze-drying process. These hybrids display excellent flexibility and steady compression-resilience properties and also the special three-dimensional structure with ultralow density of only 5–7 mg cm^{-3} shows higher EM absorption than most foam-based EM absorbers. Studies have shown that the minimum reflection loss of CF/MXene-N2 reaches −45 dB at 8.8 GHz with the $Ti_3C_2T_X$ nanosheets content of 9.8%. In the meanwhile, the effective absorption bandwidth of CF/MXene-N2 can also reach up to 5 GHz (from 6.9 GHz to 11.9 GHz) with the thickness of 4.5 mm. Moreover, the fundamental EM absorption mechanism of CF/MXene hybrids involved to impedance matching, conductive loss and polarization loss is carefully analyzed. Thus, it is expected that the new ultralight carbon foam/$Ti_3C_2T_X$ hybrids with three-dimensional network structure will have great application prospects in the fields of EM absorption.

Introduction

In today's society, with the rapid development of electronic technology, electromagnetic (EM) waves have become a new environmental pollutant and threat, not only influencing the operation of precision instruments and military electronic equipment, but also affecting human health.[1–5] Thus, it is urgent to develop new high-performance EM absorbing materials to counteract the hazards.[6–9] As an efficient EM absorbing material, three-dimensional (3D) foam can offer ultralow density, abundant pore structure and high specific surface area, which are widely valued in EM absorption.[10–15] Reasonable structure and composition optimization are effective ways to improve the electromagnetic parameters and EM wave absorption performance. For example, Dong *et al.* modified 3D graphene foams by *in situ* growth of Si_3N_4 nanowires and SiC nanowires respectively by carbon thermal method, and obtained excellent EM wave absorption effects.[13] Ye *et al.* introduced a novel three-dimensional SiC/carbon-silica aerogel foam, which was fabricated by chemical vapor deposition and the sol–gel method, showing a minimum reflection loss of −18.41 dB at 16.92 GHz with the thickness of 3.65 mm.[14] However, the effective absorption bandwidth of this foam was only 1.7 GHz, ranged from 15.80 to 17.52 GHz.

The carbon-based material, especially carbon foam (CF) with chemical stability, low density, high porosity and large surface area, is a promising EM wave absorber and carrier, which has attracted a lot of attention in recent years.[15–19] Yang *et al.* investigated the EM absorption properties of mesophase pitch CF by low temperatures treatment.[20] It was found out that the pure CF showed weak EM wave absorption performance owing to low dielectric loss. Wang *et al.* reported a facile template method to prepared an electromagnetic functionalized lightweight CF, which induced the magnetic Fe species in the formation of CF.[21] Zhao *et al.* indicated that the EM absorbing properties of the CF can be significantly improved by introducing Ni nanoparticles into the CF skeleton, owing to the derived interface polarization loss, conductivity loss, weak magnetic loss, and porosity, which have large electromagnetic absorption.[22] Therefore, modification of CF is necessary in special fields such as absorbing wave.

As recently reported, $Ti_3C_2T_X$ MXene, as a new type of two-dimensional (2D) materials have attracted tremendous attention in the EM field, owing to their unique 2D laminated structure, ultrahigh electrical conductivity (>4600 S cm^{-1}), active functional groups (–OH, =O, –F) and native defects.[23–27] Typically, Li *et al.* reported the excellent EM absorption performance of ultralight $Ti_3C_2T_X$/SiC nws hybrid foams, showing the minimum reflection loss of −55.7 dB and the effective absorption bandwidth of whole X-band at the thickness of 3.5–3.8 mm.[28] Qian *et al.* reported that the EM absorbing performance of ZnO-MXene $Ti_3C_2T_X$ nanocomposite is

[a]College of Materials Science and Engineering, Nanjing Tech University, Nanjing 210009, China. E-mail: yangjian1976@163.com; Tel: +86 13605191742

[b]Jiangsu Collaborative Innovation Center for Advanced Inorganic Function Composites, Nanjing Tech University, Nanjing 210009, China

[c]Jiangsu Collaborative Innovation Center for Advanced Inorganic Function Composites, Nanjing University of Aeronautics and Astronautics, Nanjing 210016, China

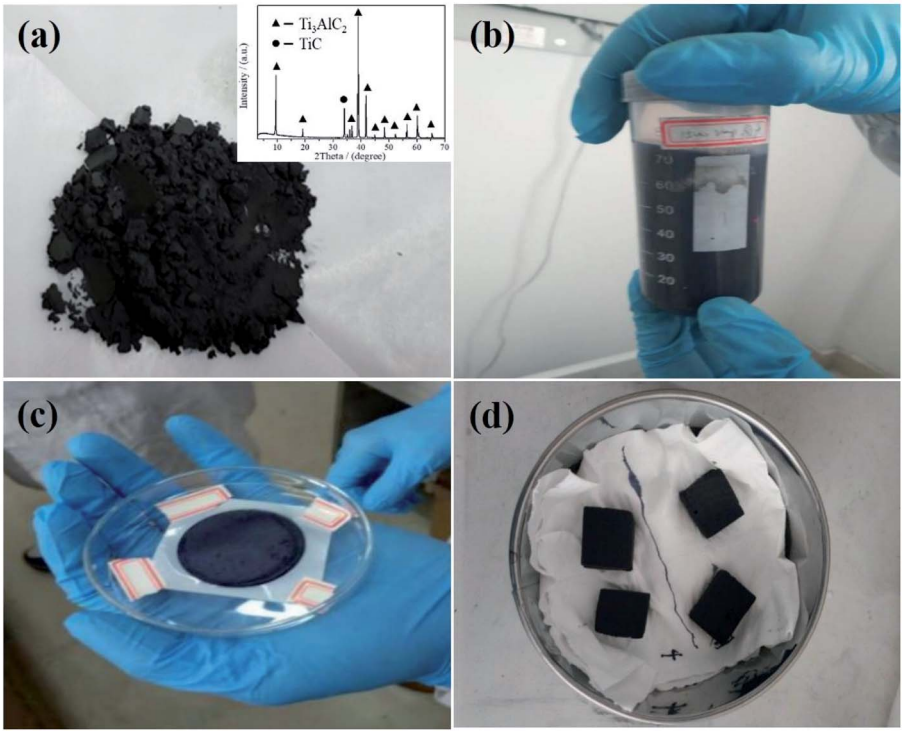

Fig. 1 As-prepared Ti_3AlC_2 MAX powder (a); f-$Ti_3C_2T_X$ solution (b); f-$Ti_3C_2T_X$ film (c); as-prepared CF/MXene and CF samples (d).

significantly better than that of pure $Ti_3C_2T_X$, owing to the unique networks structure and more interfaces.[29] Tong *et al.* found that the $Ti_3C_2T_X$/PPy hybrids exhibited a minimum reflection loss of −49.2 dB at the thickness of 3.2 mm and an effective absorption bandwidth of 4.9 GHz corresponding to the thickness of 2.0 mm.[30] From the above, the $Ti_3C_2T_X$ Mxene

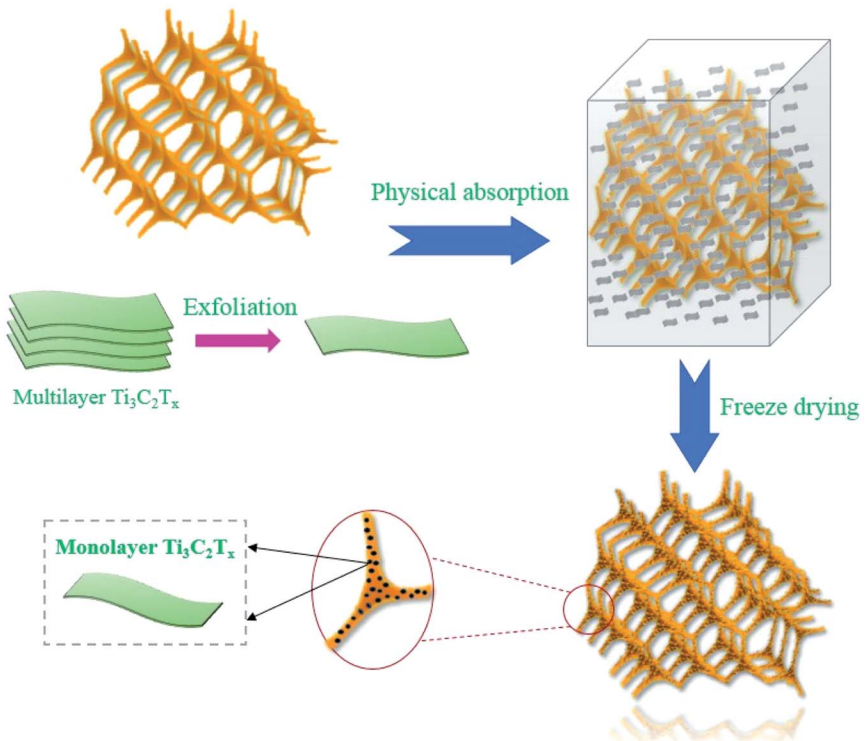

Fig. 2 Schematic illustrating the fabrication of carbon foam/$Ti_3C_2T_X$ hybrids.

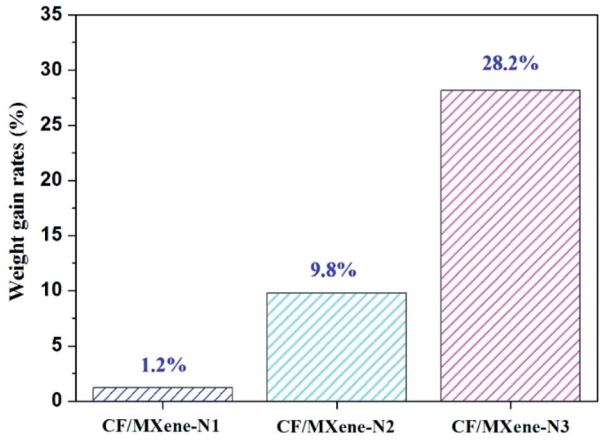

Fig. 3 Different contents of adsorbed $Ti_3C_2T_X$ nanosheets in CF/MXene-N1, CF/MXene-N2 and CF/MXene-N3.

hybrids with designed microstructure can enhance the comprehensive performance of electromagnetic wave absorption obviously.

Herein, we combine the advantages of CF and MXene to prepare a new flexible and ultralight carbon foam/$Ti_3C_2T_X$ MXene hybrids by vacuum impregnation and freeze-drying process, which is simple and efficient for large-scale fabrication. For the hybrids, CF provides a 3D network skeleton with excellent flexibility and steady compression-resilience properties, and the few-layered $Ti_3C_2T_X$ nanosheets are attached to the surface of skeleton uniformly, which can be served as polarizing sites. In addition, the EM absorption performance of carbon foam/$Ti_3C_2T_X$ MXene hybrids and related EM loss mechanisms are fully investigated in the frequency of 2–18 GHz. This work provides the great potential of ultralight carbon foam/$Ti_3C_2T_X$ MXene hybrids as ideal candidates in the field of EM absorption.

Experimental

Preparation of carbon foam and Ti_3AlC_2 (MAX) powder

Melamine foam (MF; Chengdu Yulong Chemical Co,. Ltd, China) acted as the precursor of CF, a commercially available polymer foam with high porosity of over 99% and low density in the range of 4–8 mg cm^{-3}. The MF was carbonized in vacuum tube furnace at 1100 °C with a heating rate of 3 °C min^{-1} and holding for about 2 h to get the stable CF sample with a great volume shrinkage. It should be note that when the temperature was heated between 380 °C and 400 °C, MF began to decompose violently, a large number of small molecules overflowed and the network structure became unstable. Therefore, slow heating is beneficial to maintain the stability of the skeleton structure. After that, the density of the obtained CF is about 5 mg cm^{-3} with extremely high porosity of 99.6%.

Ti_3AlC_2 (MAX) powder was prepared by high-temperature sintering of TiC powder, Ti powder and Al powder (≥99%; Alfa Aesar; USA) after ball milling. First, weigh TiC, Ti powder, Al powder with a molar ratio of 2 : 1 : 1, and ball mill for 24 h. Then, the mixed powder was calcined at 1400 °C under an inert atmosphere for 2 hours to obtain Ti_3AlC_2 block. Finally, the block was manually ground and passed through a 200 mesh sieves to obtain Ti_3AlC_2 powder as shown in Fig. 1(a). By XRD analysis, the obtained Ti_3AlC_2 powder contained a small amount of TiC, which can be used in subsequent experiments.

Preparation of few-layered $Ti_3C_2T_X$ MXene nanosheets

The few-layered $Ti_3C_2T_X$ nanosheets denoted as f-$Ti_3C_2T_X$ were fabricated *via* a facile synthesis process.[31] First of all, 1 g LiF

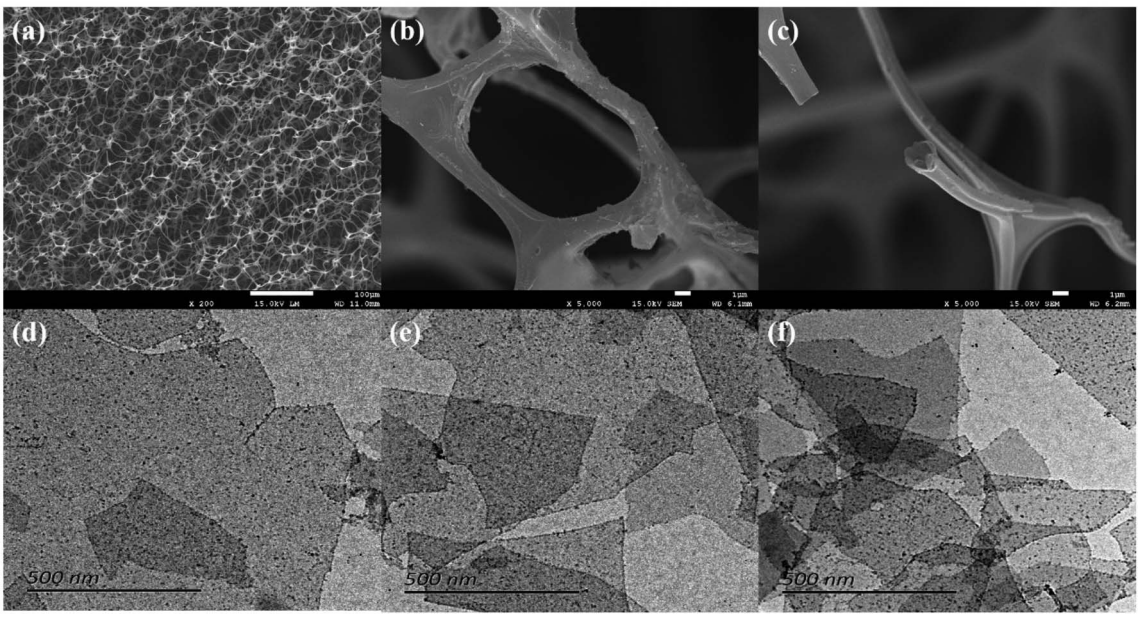

Fig. 4 Typical microstructure SEM images of carbon foam (a–c); TEM images of $Ti_3C_2T_X$ suspension with 0.2 mg ml^{-1} (d), 1 mg ml^{-1} (e), 3 mg ml^{-1} (f).

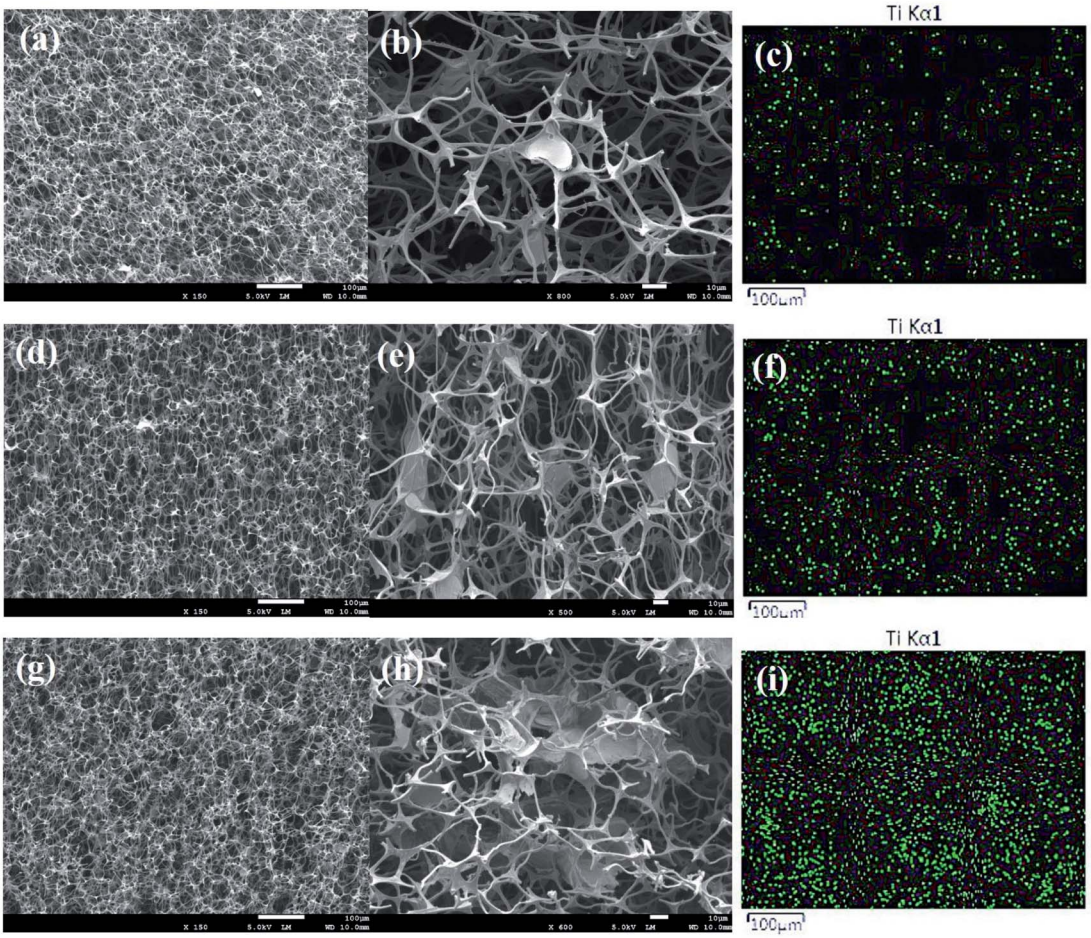

Fig. 5 Microstructure of CF/MXene-N1 (a), CF/MXene-N2 (d), CF/MXene-N3 (g); magnification of local region in CF/MXene-N1 (b), CF/MXene-N2 (e), CF/MXene-N3 (h); EDS map analysis of CF/MXene-N1 for Ti element (c); CF/MXene-N2 for Ti element (f), CF/MXene-N3 for Ti element (i).

powder (≥99%; Alfa Aesar; USA) was dissolved in 20 ml HCl solution with a concentration of 9 mol L^{-1} (Aladdin reagent), followed by stirring for about 10 min until the LiF is completely dissolved at room temperature. After that, slowly pour 1 g Ti_3AlC_2 MAX powder into the above solution. Then, the solution was stirring for 24 h in a 35 °C water bath with sealed condition. After 24 h, the solution was washed 3 times with deionized water and 2 times with alcohol (Aladdin reagent) by centrifugal treatment (3500 rpm and 5 min for each cycle) until the pH of the solution reached 6–7. Finally, the sediment was subjected to ultrasonic oscillation in deionized water for 1 h and centrifuged for 1 h with 3500 rpm. At the end of the centrifugation, the upper dark green suspension was the f-$Ti_3C_2T_X$ solution as shown in Fig. 1(b). A certain volume of upper dark green suspension was filtered into a film to measure the weight (Fig. 1(c)), which was used to calculate the concentration of the obtained f-$Ti_3C_2T_X$ suspension. According to the calculation, the initial concentration of f-$Ti_3C_2T_X$ suspension was 3 mg ml^{-1}. Subsequently, the f-$Ti_3C_2T_X$ suspension of 3 mg ml^{-1}, 1 mg ml^{-1} and 0.2 mg ml^{-1} were separately prepared by adding deionized water to dilute the original f-$Ti_3C_2T_X$ suspension.

Preparation of carbon foam/f-$Ti_3C_2T_X$ hybrids

The carbon foam/f-$Ti_3C_2T_X$ hybrids as shown in Fig. 1(d) denoted as CF/MXene were prepared *via* vacuum impregnation and freeze-drying process. The key fabrication process is shown in Fig. 2. First, four as-prepared CF samples were placed in four vacuum vessels. Three of the CF samples were inhaled with 0.2 mg ml^{-1}, 1 mg ml^{-1}, 3 mg ml^{-1} f-$Ti_3C_2T_X$ suspensions, respectively. For the contrast, another CF sample was inhaled with deionized water. After that these samples were taken out and put into a beaker. Liquid nitrogen was slowly poured to the beaker and immersed the four samples until the residual solution inside the foam was completely frozen. Then, the samples were transferred an airtight container for vacuum drying under 0.1 Pa pressure. After 24 h, the CF/MXene samples were obtained and named as CF/MXene-N1, CF/MXene-N2, CF/MXene-N3 respectively to the different concentration of impregnation f-$Ti_3C_2T_X$ solution (0.2 mg ml^{-1}, 1 mg ml^{-1}, 3 mg ml^{-1}). Meanwhile, the contents of adsorbed $Ti_3C_2T_X$ nanosheets in CF/MXene-N1, CF/MXene-N2 and CF/MXene-N3 can be expressed by their weight gain rates (the weight of adsorbed $Ti_3C_2T_X$ nanosheets divided by the weight of original carbon foam), which were measured by using a high-precision balance

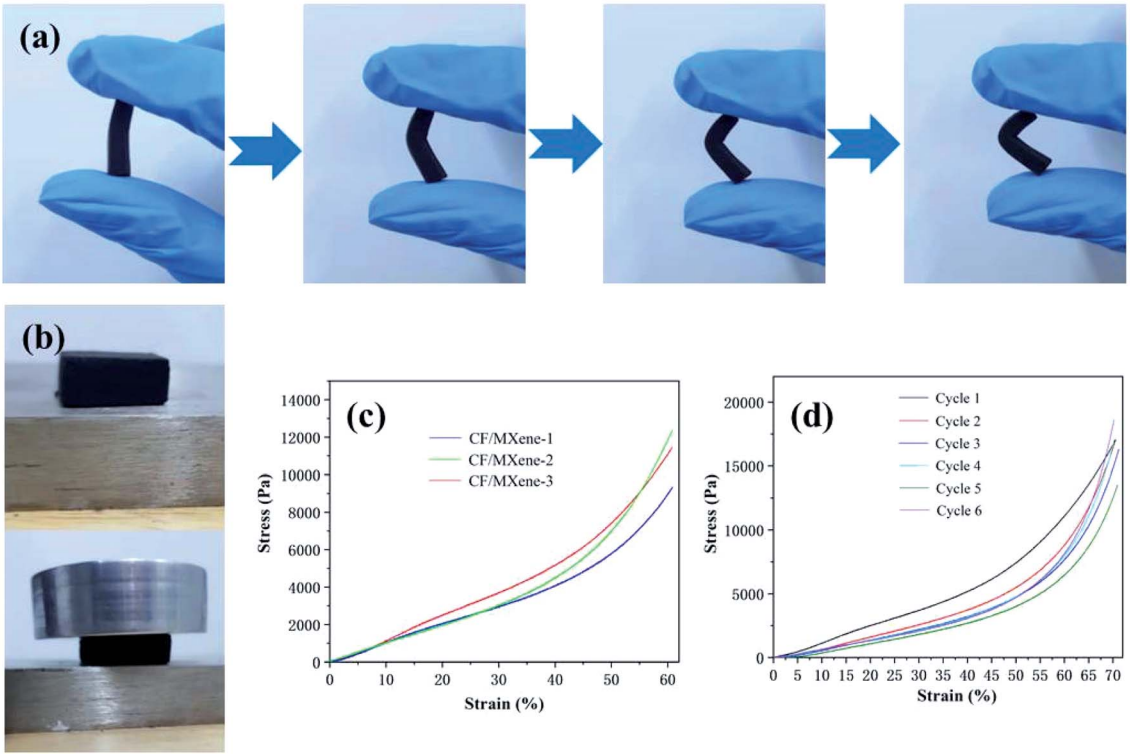

Fig. 6 (a) Optical image of the bendability of CF/MXene hybrids, (b) compressibility of CF/MXene hybrids, (c) the stress–strain curves of CF/MXene-1, CF/MXene-2 and CF/MXene-3, (d) the stress–strain curves of CF/MXene-3 within 6 cycles.

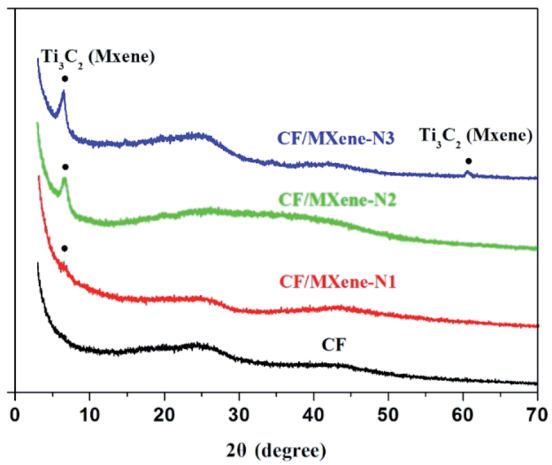

Fig. 7 XRD patterns of CF, CF/MXene-N1, CF/MXene-N2 and CF/MXene-N3.

and shown in Fig. 3. The higher the weight gain rate, the more f-$Ti_3C_2T_X$ nanosheets are adsorbed in samples.

Characterization

X-ray diffraction (XRD; SmartLab, Japan) is used to analyze the phase composition of the samples with a range of 5–70° and a step scan of 0.02° per step. The 3D network microstructures and $Ti_3C_2T_X$ nanosheets were characterized by scanning electron microscopy (SEM; JEM-2100F, Japan), and transmission electron microscopy (TEM; JEM 2100, Japan). Compression performances of the samples were tested by electron universal testing machines (CMT-8102, China). The specific surface area (SSA) of the freeze-drying CF/MXene samples were measured on nitrogen adsorption instrument (Belsorp-max, USA) at 77 K, the calculated SSA values were based on the Brunauer–Emmett–Teller (BET) method. The vector network analyzer (Agilent, N5244A) was employed to test the electromagnetic parameters of the CF/MXene-wax composite using the transmission/reflection method. In addition, the reflection loss was calculated by the transmission method within the frequency of 2–18 GHz.

Results and discussion

The morphologies and microstructures of CF and $Ti_3C_2T_X$ MXene nanosheets are revealed in Fig. 4. Fig. 4(a) shows the as-prepared CF with porous and isotropic structure. Fig. 4(b and c) exhibit the in-depth structural details of CF. It can be seen clearly that the pore size is between 20–40 μm and the size of the skeleton is about 2 μm. The carbon skeleton with extremely high aspect ratio of 10–20 makes CF have excellent flexibility. Meanwhile, the CF has a large specific surface area and low density, which can be used as a substrate for carrying $Ti_3C_2T_X$ nanosheets. Fig. 4(d–f) shows the TEM images of $Ti_3C_2T_X$ nanosheets with different concentrations of suspensions. It can be seen that the aggregation and stacking effect of $Ti_3C_2T_X$ nanosheets with the sizes between 500 and 1000 nm becomes

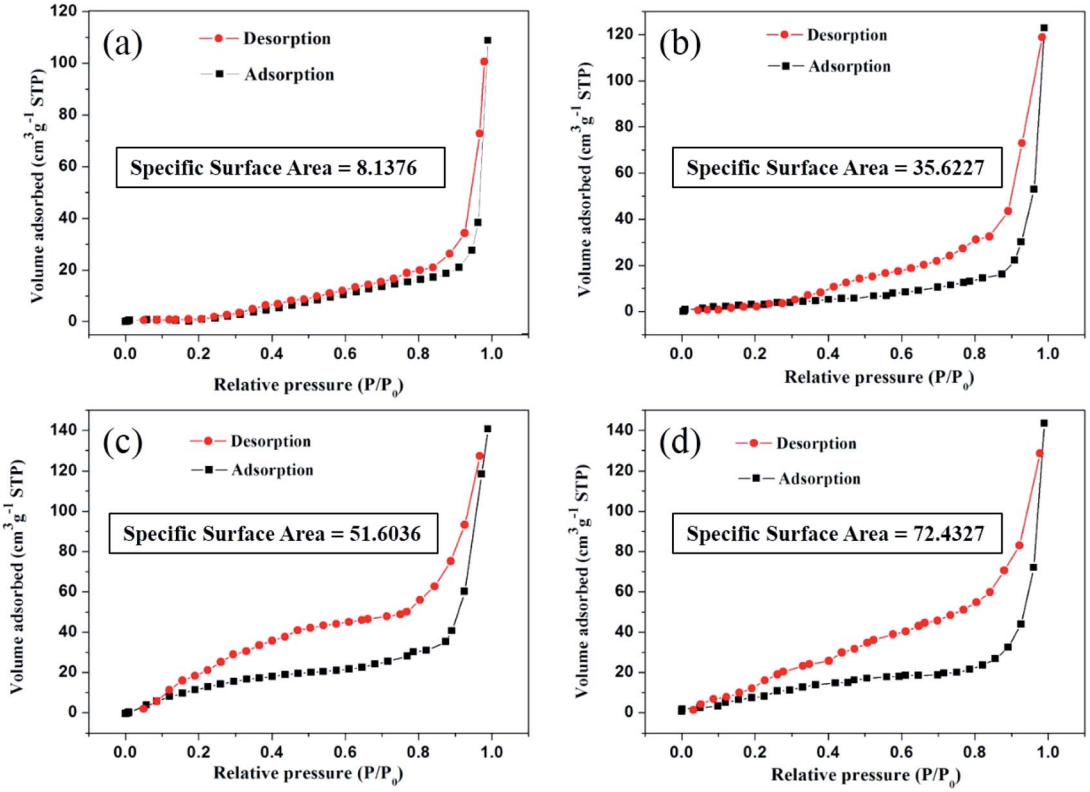

Fig. 8 N_2 adsorption–desorption isotherms of CF (a), CF/MXene-N1 (b), CF/MXene-N2 (c) and CF/MXene-N3 (d).

more pronounced as the concentration of MXene suspension increases from 0.2 mg ml^{-1} to 3 mg ml^{-1}.

Fig. 5(a, d and g) show the cross-sectional microstructure of CF/MXene-N1, CF/MXene-N2 and CF/MXene-N3. It can be seen that the CF/MXene samples still maintain the 3D skeleton structure with high porosity (about 99.4%) and the ultralow densities of only 5–7 mg cm^{-3}. The magnified images in Fig. 5(b, d and f) show the distribution of $Ti_3C_2T_X$ nanosheets in the CF. For CF/MXene-N1, $Ti_3C_2T_X$ nanosheets are sparse in CF as shown in Fig. 5(b), but for CF/MXene-N2 and CF/MXene-N3, the content of $Ti_3C_2T_X$ nanosheets are gradually increasing (Fig. 5(e and h)). A large amount of flake-like $Ti_3C_2T_X$ MXene is present inside the CF, which is not only attached to the surface of the carbon skeleton but also filled in the cells of the CF. EDS map analysis Ti element was used to determine the distribution of $Ti_3C_2T_X$ nanosheets in the samples. The distribution of Ti element in the foam skeleton in Fig. 5(c) is very rare and uniform, indicating that the content of $Ti_3C_2T_X$ nanosheets in CF/MXene-N1 is sparse but uniform. As can be seen from Fig. 5(f and i), the distribution of Ti element becomes denser, indicating that the content of $Ti_3C_2T_X$ nanosheets is gradually higher. More important, the distributions of $Ti_3C_2T_X$ nanosheets in CF/MXene-N2 and CF/MXene-N3 are still fairly uniform.

In Fig. 6(a), a CF/MXene specimen is bent over 90° and still has no fracture, showing excellent flexibility. This is mainly because the CF/MXene still retains the 3D structure and the high aspect ratio of the CF, which shown in Fig. 5(b, e and h). Moreover, the CF/MXene specimen can also be compressed without cracking as shown in Fig. 6(b). Fig. 6(c) shows typical elastic compressive stress–strain curves of CF/MXene-1, CF/MXene-2 and CF/MXene-3. It can be seen that even if the strain of the three samples exceeds 60%, there is no break. During the experiment, the CF/MXene-3 sample was compressed by 70% and then unloaded. After the sample was restored to its original shape, it was continuously pressed 6 times with the same strain cycle, and the stress–strain curve was measured each time as shown in Fig. 6(d). It can be seen that the stress of the sample did not decrease significantly, indicating the CF/MXene sample has excellent resilience and flexibility.

Fig. 7 shows the XRD patterns of CF, CF/MXene-N1, CF/MXene-N2 and CF/MXene-N3. It can be seen that CF has no obvious diffraction peak, indicating the CF is a kind of amorphous carbon.[32] In addition, CF/MXene-N1, CF/MXene-N2 and CF/MXene-N3 samples show the characteristic peaks at 7.17° corresponding to the f-$Ti_3C_2T_X$ peak of (002) plane.[33] However, as the content of $Ti_3C_2T_X$ nanosheets in CF/MXene decreased, the diffraction peaks intensity of $Ti_3C_2T_X$ gradually decreased.

Fig. 8 shows the N_2 adsorption–desorption isotherms of CF, CF/MXene-N1, CF/MXene-N2 and CF/MXene-N3 samples that have changed greatly with the different content of $Ti_3C_2T_X$ nanosheets. Calculation suggests that the SSA value of CF is 8.1376 m^2 g^{-1}. However, after adsorbing $Ti_3C_2T_X$ nanosheets, the values of CF/MXene-N1, CF/MXene-N2 and CF/MXene-N3 specific surface area are significantly increased, reaching up

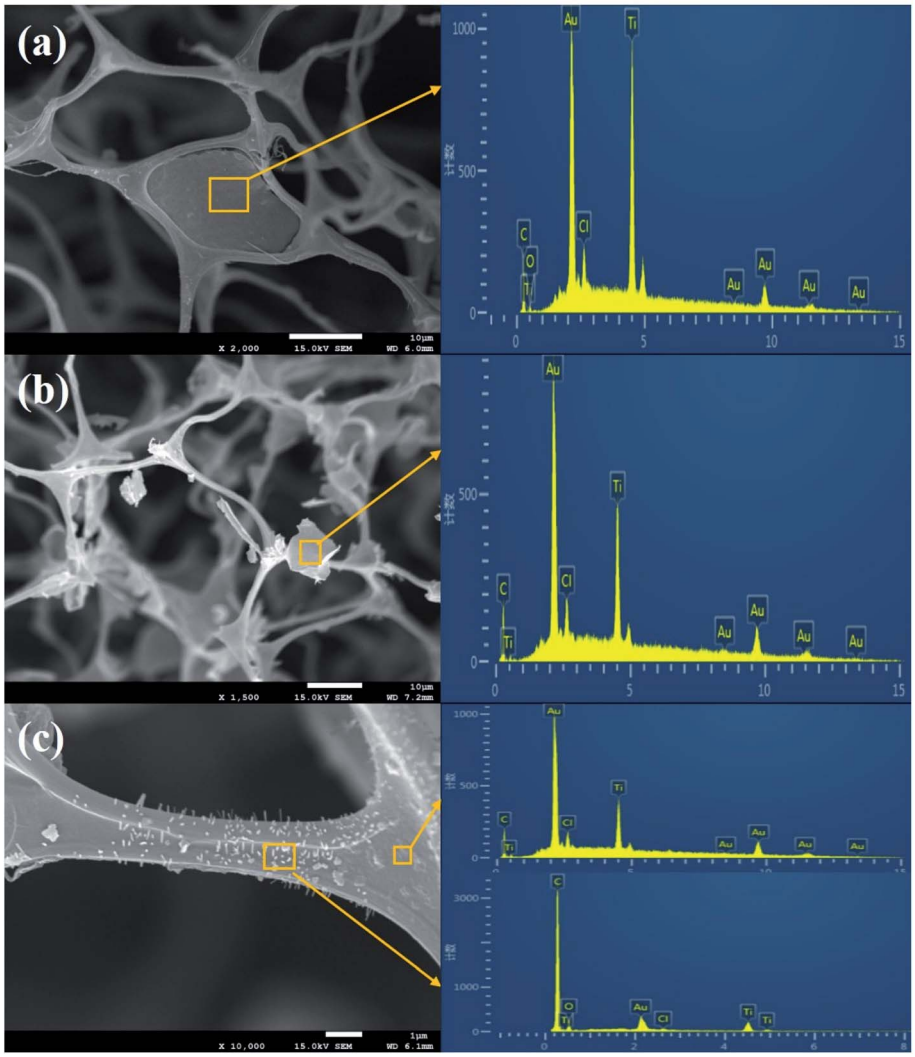

Fig. 9 Three typical states of $Ti_3C_2T_X$ nanosheets in the hybrids; (a) $Ti_3C_2T_X$ MXenes cover the CF micropores, (b) $Ti_3C_2T_X$ MXenes hang on the CF skeleton, (c) $Ti_3C_2T_X$ MXenes attach to the surface of the CF skeleton.

to 35.6227 $m^2\ g^{-1}$, 51.6036 $m^2\ g^{-1}$ and 72.4327 $m^2\ g^{-1}$, respectively, which are 4–9 times more than that of pure CF. The increased SSA due to the abundant interfaces and defects is beneficial to EM dissipation.[34] Therefore, the introduction of $Ti_3C_2T_X$ nanosheets into CF is benefit to improve the absorption efficiency of EM waves.

Fig. 9 shows three typical states of $Ti_3C_2T_X$ nanosheets in CF/MXene samples. In Fig. 9(a), a film formed by agglomeration of $Ti_3C_2T_X$ nanosheets covers the whole micropores of CF. Meanwhile, the O and Cl elements peaks are detected in the result of EDS analysis, indicating the Cl^- and O^{2-} functional groups are present in the prepared $Ti_3C_2T_X$ MXene. In addition, the existence of the Au element is due to the gold sputtering process. As shown in Fig. 9(b), some small sized $Ti_3C_2T_X$ nanosheet aggregates verified by EDS hang on the CF skeleton. In Fig. 9(c), a large number of $Ti_3C_2T_X$ nanosheets arranged in a vertical array or in a flat arrangement closely attach to the CF skeleton. The three states of $Ti_3C_2T_X$ nanosheets in the hybrids are formed during the freeze-drying process, which are affected by the $Ti_3C_2T_X$ suspension concentration and the freezing rate. It should be noted that the $Ti_3C_2T_X$ nanosheets or aggregates are isolated from each other, which makes it possible to generate local electric fields and polarization, thereby facilitating the absorption of EM waves.

The relative complex permittivity of CF/MXene and CF samples, including the real part ε', imaginary part ε'', and tangent loss tan $\delta = \varepsilon''/\varepsilon'$, was investigated in the coverage frequency ranging from 2 to 18 GHz, as shown in Fig. 10. The ε' represents the ability to store electromagnetic waves, while the ε'' represents the ability to consume electromagnetic waves. As illustrated in Fig. 10(a and b), the ε' and ε'' values show a downward trend at the same time with the increase of the frequency obviously. In Fig. 10(a), the ε' are increasing with the increase of the $Ti_3C_2T_X$ nanosheet contents, while for the ε'', the values increase first, and then decrease as shown in Fig. 9(b). In addition, there is a significant difference between CF and the CF/MXene samples, the ε'' and ε'' values of CF sample are lowest, indicating that its EM absorbing performance is weaker

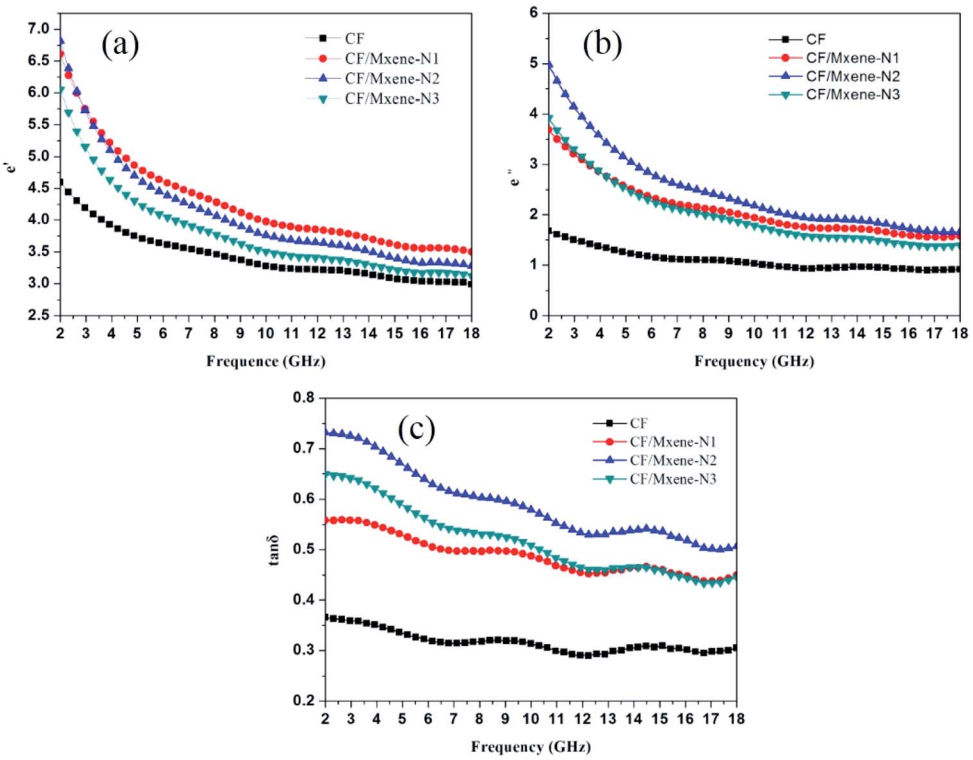

Fig. 10 Frequency dependence of (a) the real part ε' and (b) imaginary part ε'', (c) tangent loss (tan δ).

than others. Based on the Debye theory, ε' and ε'' were calculated by the following equations:[14,35]

$$\varepsilon' = \varepsilon_\infty + (\varepsilon_s - \varepsilon_\infty)/(1 + \omega^2\tau^2) \quad (1)$$

$$\varepsilon'' = (\varepsilon_s - \varepsilon_\infty)\omega\tau/(1 + \omega^2\tau^2) + \sigma_{ac}/\omega\varepsilon_0 \quad (2)$$

where ε_s is the static permittivity, and ε_0 is the dielectric constant in vacuum, ε_∞ is the high-frequency limit relative dielectric permittivity, ω is the angular frequency, σ_{ac} is the alternative conductivity and τ is the polarization relaxation time.

What is more, Fig. 10(c) also shows the variation tendency of tan δ values, which represent the EM dissipation capability of different samples.[28,36] It can be seen the EM dissipation capability enhanced significantly with the addition of $Ti_3C_2T_X$ nanosheets, but if the content of $Ti_3C_2T_X$ nanosheets is too high, the tan δ values will decrease again, as shown in the curve of CF/MXene-N3. In fact, EM absorption performance not only relates to the dissipation of EM waves, but also closely depends on the impedance matching, which determines the ability of incident EM to enter the absorber.[37,38] Z_{in} values represent the input impedance at the interface between the air and the absorber based on the transmission line theory in eqn (3).[39,40]

$$Z_{in} = (\mu/\varepsilon)^{1/2} \tanh[j(2\pi fd/c)(\mu\varepsilon)^{1/2}] \quad (3)$$

where constants c is the light velocity, f represents EM frequency (2–18 GHz), d is the thickness of the absorbers, ε and μ indicate the permittivity and permeability. And $|Z_{in} - 1|$ reflects the impedance matching characteristics. The closer the value of $|Z_{in} - 1|$ are to zero, the better the impedance matching of absorbers is.

Reflection loss values (RL) of CF, CF/MXene-N1, CF/MXene-N2 and CF/MXene-N3 represent the EM absorption performance of samples, which has been demonstrated in Fig. 11. In general, a material with an RL value of <-10 dB is considered to be an effective EM absorber, which means that >90% incident EM is absorbed and the corresponding frequency range is called the effective absorption bandwidth (EAB).

Fig. 11(a and b) shows the 3D representations and curves variation of RL values with thickness (0–5 mm) and frequency (2–18 GHz) of CF. Clearly, the RL values of the CF don't reach -10 dB in the whole frequency range at any thickness, which indicate the EM absorption performance of CF is poor. Remarkably, with the addition of $Ti_3C_2T_X$ nanosheets, the EM absorption performance of CF/MXene-N1 is significantly improved, as illustrated in Fig. 10(c and d). When the matching thickness is 5 mm, the minimum RL (RL_{min}) goes up to -24.6 dB at 8 GHz with the effective absorption bandwidth (EAB) of 4.5 GHz from 6.7 GHz to 11.2 GHz. It can also be seen from Fig. 11(d) that the RL_{min} transfers to a lower frequency with increasing matching thickness according with the law of quarter-wavelength attenuation.[41–43] More importantly, the EAB is always wide enough, when the thicknesses distribute between 3 and 5 mm. For the CF/MXene-N2, as shown in Fig. 10(e and f), the RL_{min} is further reduced to -45 dB at 8.8 GHz with the thickness of 4.5 mm, demonstrating superior EM absorbing performance. What is more, the EAB can also reach up to 5 GHz

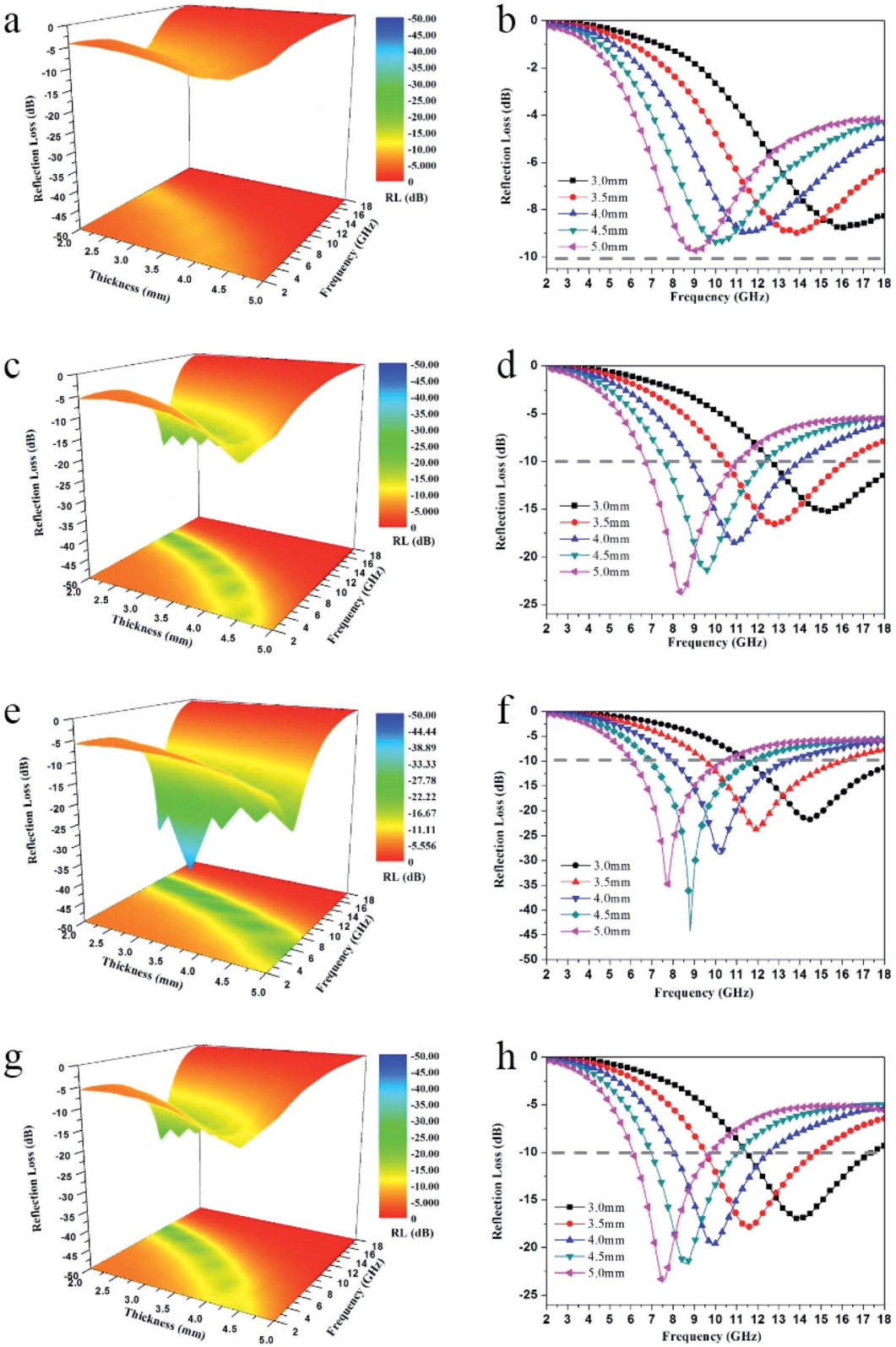

Fig. 11 Three-dimensional representations and RL curves *vs.* frequency (2–18 GHz) and thickness (0–5 mm) of CF (a) and (b), CF/MXene-N1 (c) and (d), CF/MXene-N2 (e) and (f) and CF/MXene-N3 (g) and (h).

(6.9–11.9 GHz). This is because more $Ti_3C_2T_X$ nanosheets adsorbing on the CF skeleton further increase the specific surface area, resulting in more defects and interfaces, which is more conducive to the dissipation of EM waves. However, for CF/MXene-N3 as shown in Fig. 11(g and h), the RL_{min} values increase to −24.1 dB at the thickness of 5 mm, indicating the

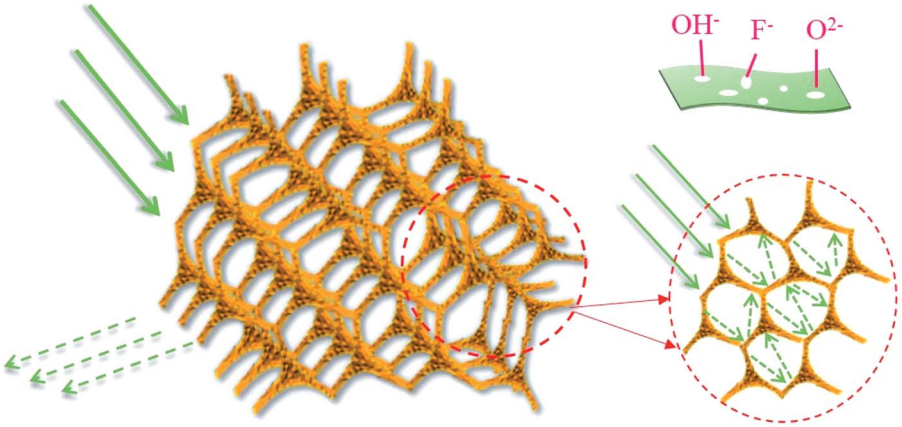

Fig. 12 Schematic illustrating the EM absorption mechanisms of carbon foam/$Ti_3C_2T_X$ hybrids.

Table 1 EM absorption of representative foam-bases composites

			RL ≤ −10 dB			
Sample	Matrix	Density (g cm^{-3})	d (mm)	EAB (GHz)	RL_{min} (dB)	Ref.
RGO foam	Wax	0.9	10	4.2	−27.0	3
RGO/PPy/Fe_3O_4	Wax	0.900	3	4.2	−49.2	11
SiC/CF-aerogel	Wax	0.112	3.5	1.6	−18.4	14
RGO/SiC_{nws} foam	PDMS	0.097	3.00	4.2	−19.6	19
C foam	Epoxy	1.600	1.2	2.0	−10.0	20
C/Fe foam	Air	0.130	10.4	0.2	−45.0	21
$Ti_3C_2T_X$/SiCnws foams	None	0.029	3.5–3.8	4.2	−55.7	28
Fe_3O_4/TiO_2/EP	Epoxy	1.600	1.2	4.2	−22.0	36
C/SiC_{nws} foam	Epoxy	1.600	3.30	4.2	−31.0	48
RGO/CNT foam	PDMS	0.097	2.75	3.5	−55.0	49
RGO/ZnO_{nws} foam	PDMS	0.097	4.8	4.2	−27.8	50
CF/MXene-N2	Wax	0.006	4.5	5	−45.0	This work

further increase of $Ti_3C_2T_X$ nanosheets is not conducive to the absorption of EM waves. The decrease of absorbing performance of CF/MXene-N3 can be attributed to the bad impedance matching, which is caused by the high conductivity of excess $Ti_3C_2T_X$ nanosheets.

Fig. 12 presents the associated EM absorption mechanism of carbon foam/$Ti_3C_2T_X$ hybrids. 3D CF provides a large number of micropores, not only reduces the density but also effectively prevent the agglomeration of $Ti_3C_2T_X$ nanosheets. First, the $Ti_3C_2T_X$ nanosheets deposited on the surface of CF skeleton can provide more surface area and interface structure. At the same time, the 3D structure greatly increases the propagation path of EM waves, causing the incident EM waves to be attenuated through zigzag reflection and scattering.[44,45] Second, the residual OH^-, F^- and O^{2-} functional groups and localized defects in $Ti_3C_2T_X$ nanosheets act as polarized centers.[46,47] Third, there is a large amount of electron migration at the defects and interfaces between $Ti_3C_2T_X$ nanosheets and CF skeleton in the alternated EM environment, thereby forming a rich field-induced microcurrent.[28] Furthermore, the microcurrents improves the conductivity and enhance the conductive loss. However, the increased conductivity with the increasing content of $Ti_3C_2T_X$ nanosheets will inevitably lead to a bad impedance matching, resulting in a decline in the overall EM absorption performance. This can explain the reason of the EM absorption performance degradation for CF/MXene-N3.

Table 1 summarizes and compares the representative foam-based EM absorption materials reported in recent years. It can be seen the RGO foam has ultra-low density, but the thickness is high reached to 10 mm. The C/Fe foam and RGO/CNT foam have excellent absorption intensity, but their density is relatively high, and the EAB is narrow. Notably, the CF/MXene-N2 in this work possesses better EM absorption performance than most current foam-based EM absorbers, which has strong absorption intensity (RL_{min} = −45.0 dB), broad EAB (5.0 GHz), ultra-low density (only 0.006 g cm^{-3}) and low thickness (4.5 mm), indicating the carbon foam/$Ti_3C_2T_X$ hybrids have a huge potential as an excellent EM absorption materials.

Conclusions

In summary, a new flexible and ultralight carbon foam/$Ti_3C_2T_X$ MXene hybrid was prepared by vacuum impregnation and freeze-drying process. The $Ti_3C_2T_X$ nanosheets are uniformly

dispersed inside the 3D CF, which significantly increases the specific surface area of the hybrid. Also, the hybrid has excellent resilience and flexibility, even if the strain exceeds 70% after 6 cycles. This is mainly because the CF/MXene hybrid retains the 3D structure and the high aspect ratio of the carbon skeleton. For the CF/MXene-N2, when the content of $Ti_3C_2T_X$ nanosheets is 9.8%, the RL_{min} is significantly reduced to −45 dB at 8.8 GHz with the thickness of 4.5 mm, and the EAB can also reach up to 5 GHz, indicating the new carbon foam/$Ti_3C_2T_X$ hybrid has huge potential to be used as new high performance EM absorption materials.

Conflicts of interest

The authors declare no conflict of interest.

Acknowledgements

This work was supported by the priority Academic Program Development of Jiangsu Higher Education Institutions (PAPD), Qing Lan Project of Jiangsu Province, the Program for Chang jiang Scholars and Innovative Research Team in University (PCSIRT), IRT1146 and IRT15R35, and the Top–notch Academic Programs Project of Jiangsu Higher Education Institutions (TAPP, PPZY2015B128).

References

1 X. Liang, W. Liu, Y. Cheng, J. Lv, S. Dai, D. Tang, B. Zhang and G. Ji, *J. Alloys Compd.*, 2018, **749**, 887–899.
2 B. Dai, B. Zhao, X. Xie, T. Su, B. Fan, R. Zhang and R. Yang, *J. Mater. Chem. C*, 2018, **6**, 5690–5697.
3 Y. Zhang, Y. Huang, H. Chen, Z. Huang, Y. Yang, P. Xiao, Y. Zhou and Y. Chen, *Carbon*, 2016, **105**, 438–447.
4 W. Duan, X. Yin, Q. Li, L. Schlier, P. Greil and N. Travitzky, *J. Eur. Ceram. Soc.*, 2016, **36**, 3681–3689.
5 K. Zhang, H. O. Yu, Y. D. Shi, Y. F. Chen, J. B. Zeng, J. Guo, B. Wang, Z. Guo and M. Wang, *J. Mater. Chem. C*, 2017, **5**, 2807–2817.
6 Y. Z. Wei, G. S. Wang, Y. Wu, Y. H. Yue, J. T. Wu, C. Lu and L. Guo, *J. Mater. Chem. A*, 2014, **2**, 5516–5524.
7 X. Yin, L. Kong, L. Zhang, L. Cheng, N. Travitzky and P. Greil, *Int. Mater. Rev.*, 2014, **59**, 326–355.
8 W. Liu, H. Li, Q. Zeng, H. Duan, Y. Guo, X. Liu, C. Sun and H. Liu, *J. Mater. Chem. A*, 2015, **3**, 3739–3747.
9 J. Zhu, S. Wei, N. Haldolaarachchige, D. P. Young and Z. Guo, *J. Phys. Chem. C*, 2011, **115**, 15304–15310.
10 P. Xie, H. Li, B. He, F. Dang, J. Lin, R. Fan, C. Hou, H. Liu, J. Zhang, Y. Ma and Z. Guo, *J. Mater. Chem. C*, 2018, **6**, 8812–8822.
11 C. Zhang, Y. Chen, H. Li, R. Tian and H. Liu, *ACS Omega*, 2018, **3**, 5735–5743.
12 C. Zhang, H. Li, Z. Zhuo, R. Dugnani, C. Sun, Y. Chen and H. Liu, *RSC Adv.*, 2017, **7**, 41321–41329.
13 S. Dong, J. Song, X. Zhang, P. Hu, B. Sun, S. Zhou and X. Luo, *J. Mater. Chem. C*, 2017, **5**, 11837–11846.
14 X. Ye, Z. Chen, S. Ai, B. Hou, J. Zhang, X. Liang, Q. Zhou, H. Liu and S. Cui, *ACS Sustainable Chem. Eng.*, 2019, **7**, 2774–2783.
15 X. Sun, J. He, G. Li, J. Tang, T. Wang, Y. Guo and H. Xue, *J. Mater. Chem. C*, 2013, **4**, 765–777.
16 Y. Lu, Y. Wang, H. Li, Y. Lin, Z. Jiang, Z. Xie, Q. Kuang and L. Zheng, *ACS Appl. Mater. Interfaces*, 2015, **7**, 13604–13611.
17 C. Wang, Y. Ding, Y. Yuan, X. He, S. Wu, S. Hu, M. Zou, W. Zhao, L. Yang, A. Cao and Y. Li, *J. Mater. Chem. C*, 2015, **3**, 11893–11901.
18 F. Moglie, D. Micheli, S. Laurenzi, M. Marchetti and V. M. Primiani, *Carbon*, 2012, **50**, 1972–1980.
19 M. Han, X. Yin, Z. Hou, C. Song, X. Li, L. Zhang and L. Cheng, *ACS Appl. Mater. Interfaces*, 2017, **9**, 11803–11810.
20 J. Yang, Z. M. Shen and Z. B. Hao, *Carbon*, 2004, **6**, 1882–1885.
21 S. Wang, N. Xiao, Y. Zhou, Z. Ling, M. Li and J. Qiu, *Carbon*, 2016, **105**, 224–226.
22 H. B. Zhao, Z. B. Fu, H. B. Chen, M. L. Zhong and C. Y. Wang, *ACS Appl. Mater. Interfaces*, 2016, **8**, 1468–1477.
23 M. Naguib, V. N. Mochalin, M. W. Barsoum and Y. Gogotsi, *Adv. Mater.*, 2014, **26**, 992–1005.
24 M. Han, X. Yin, H. Wu, Z. Hou, C. Song, X. Li, L. Zhang and L. Cheng, *ACS Appl. Mater. Interfaces*, 2016, **8**, 21011–21019.
25 X. Li, X. Yin, M. Han, C. Song, X. Sun, H. Xu, L. Cheng and L. Zhang, *J. Mater. Chem. C*, 2017, **5**, 7621–7628.
26 Y. Qing, W. Zhou, F. Luo and D. Zhu, *Ceram. Interfaces*, 2016, **42**, 16412–16416.
27 M. Han, X. Yin, X. Li, B. Anasori, L. Zhang, L. Cheng and Y. Gogotsi, *ACS Appl. Mater. Interfaces*, 2017, **9**, 20038–20045.
28 X. Li, X. Yin, H. Xu, M. Han, M. Li, S. Liang, L. Cheng and L. Zhang, *ACS Appl. Mater. Interfaces*, 2018, **10**, 34524–34533.
29 Y. Qian, H. Wei, J. Dong, Y. Du, X. Fang, W. Zheng, Y. Sun and Z. Jiang, *Ceram. Int.*, 2017, **43**, 10757–10762.
30 Y. Tong, M. He, Y. Zhou, X. Zhong, L. Fan, T. Huang, Q. Liao and Y. Wang, *Appl. Surf. Sci.*, 2018, **434**, 283–293.
31 C. J. Zhang, S. Pinilla, N. McEvoy, C. P. Cullen, B. Anasori, E. Long, S. Park, A. Seral-Ascaso, A. Shmeliov, D. Krishnan, C. Morant, X. Liu, G. Duesberg, Y. Gogotsi and V. Nicolosi, *Chem. Mater.*, 2017, **29**, 4848–4856.
32 Z. Fang, C. Li, J. Sun, H. Zhang and J. Zhang, *Carbon*, 2007, **45**, 2873–2879.
33 O. Mashtalir, M. Naguib and V. N. Mochalin, *Nat. Commun.*, 2013, **4**, 1716.
34 H. Xu, X. Yin, M. Zhu, M. Han, Z. Hou, X. Li, L. Zhang and L. Cheng, *ACS Appl. Mater. Interfaces*, 2017, **9**, 6332–6341.
35 X. Liang, B. Quan, J. Chen, D. Tang, B. Zhang and G. Ji, *Sci. Rep.*, 2017, **7**, 9462.
36 J. Liu, R. Che, H. Chen, F. Zhang, F. Xia, Q. Wu and M. Wang, *Small*, 2012, **8**, 1214–1221.
37 F. X. Qin, C. Brosseau and H. X. Peng, *Chem. Phys. Lett.*, 2013, **579**, 40–44.
38 L. Quan, F. X. Qin, D. Estevez, H. Wang and H. X. Peng, *Carbon*, 2017, **125**, 630–639.
39 C. Zhou, X. Wang, H. Luo, L. Deng, S. Wei, Y. Zheng, Q. Jia and J. Liu, *Chem. Eng. J.*, 2019, 123095, DOI: 10.1016/j.cej.2019.123095.

40 C. Zhou, X. Wang, H. Luo, L. Deng, S. Wang, S. Wei, Y. Zheng, Q. Jia and J. Liu, *Appl. Surf. Sci.*, 2019, **494**, 540–550.
41 B. Zhao, G. Shao, B. Fan, W. Zhao and R. Zhang, *J. Mater. Chem. C*, 2015, **3**, 10862–10869.
42 B. Zhao, B. Fan, Y. Xu, G. Shao, X. Wang, W. Zhao and R. Zhang, *ACS Appl. Mater. Interfaces*, 2015, **7**, 26217–26225.
43 W. She, H. Bi, Z. Wen, Q. Liu, X. Zhao, J. Zhang and R. Che, *ACS Appl. Mater. Interfaces*, 2016, **8**, 9782–9789.
44 B. Zhao, X. Guo, W. Zhao, J. Deng, G. Shao, B. Fan, Z. Bai and R. Zhang, *ACS Appl. Mater. Interfaces*, 2016, **8**, 28917–28925.
45 B. Zhao, J. Deng, C. Zhao, C. Wang, Y. Chen, M. Hamidinejad, R. Li and C. Park, *J. Mater. Chem. C*, 2019, DOI: 10.1039/C9TC04575A.
46 C. Mo, L. Zhang and G. Wang, *Nanostruct. Mater.*, 1995, **6**, 823–826.
47 H. Xu, X. Yin, M. Zhu, M. Han, Z. Hou and X. Li, *ACS Appl. Mater. Interfaces*, 2017, **9**, 6332–6341.
48 S. Xiao, H. Mei, D. Han, K. G. Dassios and L. Cheng, *Carbon*, 2017, **122**, 718–725.
49 C. Song, X. Yin, M. Han, X. Li, Z. Hou, L. Zhang and L. Cheng, *Carbon*, 2017, **116**, 50–58.
50 L. Kong, X. Yin, X. Yuan, Y. Zhang, X. Liu, L. Cheng and L. Zhang, *Carbon*, 2014, **73**, 185–193.